ELSEVIER

Journal of Structural Geology 28 (2006) 887–901

JOURNAL OF STRUCTURAL GEOLOGY

www.elsevier.com/locate/jsg

# Sandbox experiments on gravitational spreading and gliding in the presence of fluid overpressures

R. Mourgues [a,b,*], P.R. Cobbold [a]

[a] *Géosciences-Rennes (UMR 6118), Campus de Beaulieu, Université de Rennes 1, Avenue du Général-Leclerc, 35042 Rennes Cedex, France*
[b] *LGRMP, Université du Maine, 72085 Le Mans Cedex 09, France*

Received 2 November 2004; received in revised form 16 December 2005; accepted 24 December 2005
Available online 29 March 2006

**Abstract**

Whereas in previous analogue experiments on gravitational spreading and gliding, detachment occurred on a ductile layer, we have used a relatively new technique of injecting compressed air into sand packs so as to simulate the effects of fluid overpressures in sedimentary strata and to trigger slope instabilities. In our experiments, the governing equations yield scales for dimensions, stresses and fluid pressure. However, the more transitory phenomena of production and decrease of overpressure cannot be suitably scaled. By using layers of differing permeability, we are able to produce sharp detachments in models made of sand alone. The experiments involve gravity spreading or gravity gliding. In gravity spreading, propagation of the detachment and of extensional deformation depends on the fluid pressure. For medium values of fluid overpressure, normal faults are closely spaced, numerous and bound rotated blocks. They propagate progressively toward the back of the model. For the highest pressures, the deformation propagates very fast and faults bound non-rotated blocks, which slide on an efficient basal detachment. Fault dips are also controlled by fluid pressure and by frictional resistance at the base. To model gravitational gliding required an apparatus with a more complex system of air injection. We did a series of experiments using injection windows of various lengths and compared the results with predictions from a quasi-3D analytical model of sliding. In contrast with predictions for an infinite slope, sliding depends on (1) the fluid overpressure on the detachment, (2) the fluid overpressure in the body of the sliding sheet, and (3) the shape of the detachment surface. In particular, we show that frictional resistance at the lower edge is a primary control on the dynamics of gliding.


*Keywords:* Fluid overpressure; Slope instability; Gravity spreading; Gravity gliding; Analogue modelling; Analytical solutions

## 1. Introduction

Gravitational gliding of the uppermost layers of sediment is a common phenomenon on continental margins and in many deltas (Fig. 1). The resulting thin-skinned deformation is visible on seismic sections as faults and folds. Some good examples have been described from the Niger Delta (Evamy et al., 1978; Damuth, 1994; Cohen and McClay, 1996), the Gulf of Mexico (Worral and Snelson, 1989), the Brazilian margin (Cobbold and Szatmari, 1991), the Gulf of Guinea (Mauduit, 1998) and the Amazon Fan (Cobbold et al., 2004).

For sediments to glide on gentle delta slopes (between 0.5 and 4°), the resistance to horizontal shearing at the base must be very small (Mandl and Crans, 1981). This will be so, for example, if there is a basal layer of ductile material, such as salt or soft sediment. Alternatively, fluid overpressure may carry part of the weight, so reducing the frictional resistance at the base. Under these conditions, the detachment may be a thin shear zone or fault (Brun and Choukroune, 1983). For the last two decades, thin-skinned gravitational deformation has been widely studied by sandbox modelling. There is a long history of using silicone putty to model salt or shale (Vendeville, 1987; Vendeville and Cobbold, 1987; Cobbold and Szatmari, 1991; Mauduit et al., 1997a,b; Mauduit, 1998; Maillard et al., 2003; Brun and Fort, 2004), assuming that these geological materials are ductile when they deform slowly (Fig. 1). In contrast, the use of pore fluids in sandbox models is more recent. Compressed air provides a practical source (Cobbold and Castro, 1999). Cobbold et al. (2001) were able to verify some of the theoretical predictions for thrust wedges containing fluid overpressures. They showed that permeability is important in controlling the positions of thin-skinned detachments. More recently, Mourgues and Cobbold (2003) have used the same

* Corresponding author. Correspondence address: LGRMP, Université du Maine, 72085 Le Mans Cedex 09, France. Fax: 33 (0)243833237.
*E-mail address:* Regis.Mourgues@univ-lemans.fr (R. Mourgues).

0191-8141/$ - see front matter © 2006 Elsevier Ltd. All rights reserved.
doi:10.1016/j.jsg.2005.12.013

**Nomenclature**

| | | | |
|---|---|---|---|
| $\sigma$ | Total stress tensor, Pa | $\mu$ | Coefficient of internal friction, – |
| $\sigma'$ | Effective stress tensor, Pa | $\mu_s$ | Coefficient of sliding (sand against wall), – |
| $q$ | Darcy velocity, m $s^{-1}$ | $c$ | Cohesion, Pa |
| $F_w$ | Weight per unit volume, N $m^{-3}$ | $K$ | Ratio of horizontal and vertical effective stress, – |
| $F_b$ | Buoyancy force per unit volume, N $m^{-3}$ | $K_s$ | Softening parameter, – |
| $F_s$ | Seepage force per unit volume, N $m^{-3}$ | $\rho_b$ | Bulk density, kg $m^{-3}$ |
| $k$ | Intrinsic permeability, $m^2$ | $\rho_s$ | Solid density, kg $m^{-3}$ |
| $\tau$ | Shear stress, Pa | $\rho_w$ | Fluid density, kg $m^{-3}$ |
| $\tau_f$ | Yield shear stress, Pa | $\phi$ | Porosity, – |
| $\sigma_n$ | Normal stress, Pa | $\alpha_b$ | Bulk compressibility, $Pa^{-1}$ |
| $P$ | Fluid pressure, Pa | $\beta$ | Compressibility of pore fluid, $Pa^{-1}$ |
| $P_d$ | Fluid pressure on detachment, Pa | $\beta_s$ | Compressibility of solid grains, $Pa^{-1}$ |
| $P_b$ | Basal fluid pressure, Pa | $\alpha$ | Slope angle, degrees (°) |
| $\lambda$ | Ratio of pore pressure and vertical stress, – | $H$ | Thickness of slide, m |
| $\lambda_b$ | $\lambda$ ratio on detachment, – | $l$ | Width of slide, m |
| $\Delta\sigma_t$ | Variation of total stress, Pa | $L$ | Length of slide, m |
| $\nabla P\|_{nh}$ | Non-hydrostatic part of the fluid pressure gradient, Pa $m^{-1}$ | | |

experimental technique for demonstrating the significance of seepage forces in tectonics.

In this paper, we further explore the potential of using compressed air. The focus is on gravity spreading and gliding in overpressured strata, as a result of slope instability. We start by discussing the scaling of sandbox models involving pore fluids. We show that granular materials such as sand are not adequate for modelling the production or diffusion of overpressure, which are transitory phenomena. On the other hand, the granular materials are valid for situations where fluid flow is steady. We briefly discuss how fluid overpressure decreases the angle of stability of a slope and we describe a series of experiments on gravity spreading, where the apparatus provides a uniform basal fluid pressure. Then we introduce a new apparatus, which allows us (1) to define the shape of an overpressured window, (2) to provide a non-uniform fluid

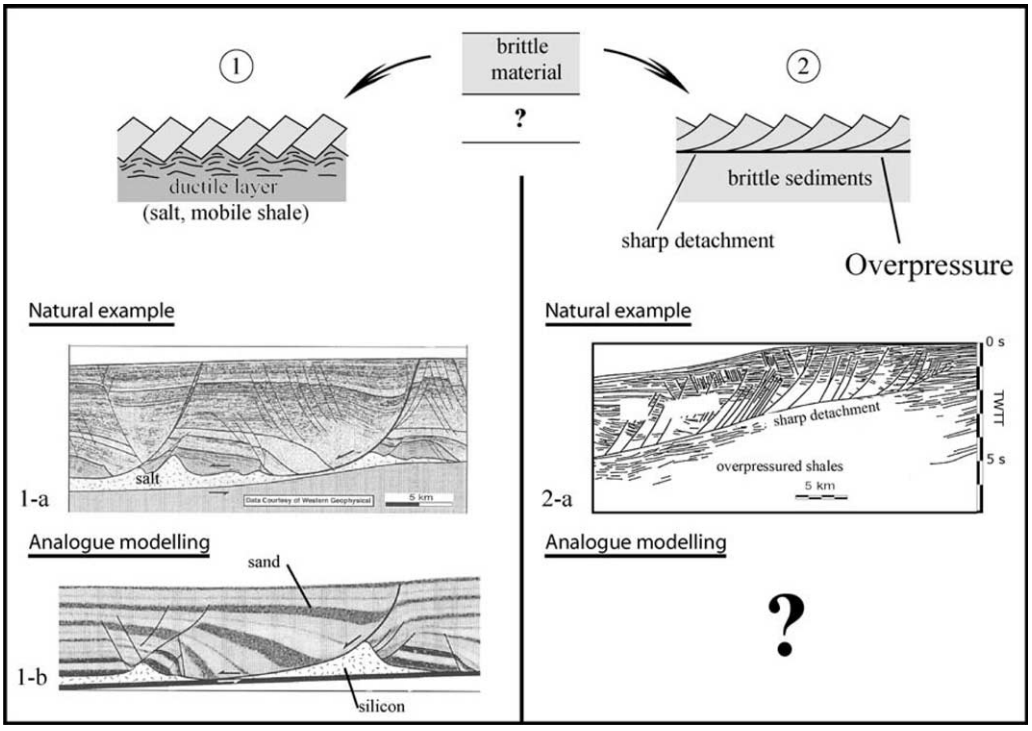


Fig. 1. Detachments involving ductile material (1) or fluid overpressures in purely brittle sediment (2). Seismic example of growth faults and salt rollers (1-a) is from the Angolan margin (after Fort, 2002). Experimental model (1-b) involves a basal layer of silicone putty (after Fort, 2002). Sharp detachment (2-c) is in overpressured shale from the Niger delta (line drawing; after Morley and Guerin, 1996). This kind of structure has not been properly modelled so far.

pressure at the base of the model, and (3) to model entire sliding sheets. Finally, we illustrate some simple experiments on gravity gliding and compare them with an analytical model of a sliding sheet. The good agreement between sandbox results and analytical predictions prepares the way for more realistic experiments in the future.

## 2. Scaling of models involving pore fluid

If pore fluids are overpressured, the main difficulty in modelling geological deformation is that the fluid pressure, fluid flow and matrix deformation are all coupled (Strayer et al., 2001). To achieve proper scaling of a deformable saturated medium, we need to consider the governing equations for the solid matrix and for the fluid.

### 2.1. Solid matrix

In terms of Cartesian coordinates, $x$, the following governing equations express the macroscopic balance of effective stresses (Terzaghi, 1923), body forces and fluid pressure gradients (Dahlen, 1990):

$$\frac{\partial \sigma'_{ij}}{\partial x_j} = \rho_b g_i - \frac{\partial P}{\partial x_i} \tag{1}$$

Here, $\sigma$ is the macroscopic effective stress tensor for the solid framework, $P$ is the macroscopic fluid pressure, $\rho_b$ is the bulk density of the aggregate, $g$ is the acceleration due to gravity, and suffixes $i$ and $j$ refer to Cartesian tensor or vector components. The bulk density is $(1-\phi)\rho_s + \phi\rho_f$, where $\phi$ is the porosity and $\rho_s$ and $\rho_f$ are the densities of solid particles and fluid, respectively.

Each parameter in Eq. (1) can be written as the product of a dimensionless variable (denoted here by a prime) and a constant reference value (denoted here by the subscript o). Eq. (1) then becomes:

$$\frac{\sigma_o}{L_o \rho_{bo} g_o} \frac{\partial \sigma'^{*}_{ij}}{\partial x^{*}_j} = \rho^{*}_b g^{*} - \frac{P_o}{L_o \rho_{bo} g_o} \frac{\partial P^{*}}{\partial x^{*}_i} \tag{2}$$

The ratios, $\sigma_o/L_o\rho_{bo}g_o$ and $P_o/L_o\rho_{bo}g_o$, are also dimensionless. They may be set to unity, by a suitable choice of reference values. On applying them to a model and its natural prototype, we obtain scaling ratios for stress and fluid pressure, in terms of scaling ratios for density, gravitational acceleration, and length, $L$:

$$\gamma_P = \frac{P_m}{P_r} = \frac{\sigma_m}{\sigma_r} = \gamma_\sigma = \gamma_L \gamma_\rho \gamma_g \tag{3}$$

where

$$\gamma_L = \frac{L_m}{L_r}, \quad \gamma_\rho = \frac{\rho_{bm}}{\rho_{br}}, \quad \gamma_g = \frac{g_m}{g_r} = 1$$

Here suffixes m and r refer to variables in model and nature, respectively. Eq. (3) lays the foundation for scale modelling in the presence of pore fluids (Cobbold et al., 2001).

To a first approximation, brittle rock and granular materials fail according to a Coulomb yield envelope, which is a linear relationship between the shear stress $\tau_f$ and the effective normal stress $\sigma'_n$ acting on a plane:

$$\tau_f = c + \mu \sigma'_n \tag{4}$$

Here $c$ is the cohesion and $\mu$ is a dimensionless coefficient of internal friction. The latter must be the same in model and nature, whereas the former scales in the same way as stress (Davy and Cobbold, 1991). If the stress ratio between model and nature is $10^{-5}$ (1 cm being equivalent to 1 km), 100 Pa for the cohesion in a model will represent a reasonable value of 10 MPa in nature (Byerlee, 1978). In our experiments, we used Fontainebleau sand. Mourgues and Cobbold (2003) obtained its yield envelope for a range of effective normal stresses, down to values as small as 5 Pa. For normal stresses greater than 30 Pa, the failure envelope for sifted sand is linear, the cohesion being smaller than 40 Pa and the coefficient of internal friction being close to 1.5. For normal stresses smaller than 30 Pa, $\mu$ increases as stress decreases, reaching a maximum of 2.5. Hence the yield envelope is not linear near the origin, but curves into it.

### 2.2. Pore fluid

In the Earth's crust, pore fluid pressure tends to increase with depth, as a result of gravity. If the pores are interconnected, the pressure gradient will be hydrostatic. This can be taken as a reference state. Overpressures (or underpressures) can develop if some mechanism disturbs this reference state. However, abnormal pressures will tend to dissipate as soon as the generating mechanism stops and provided that the rocks are permeable. In practice, therefore, overpressures are likely to be transitory (Neuzil, 1994).

For the generation of fluid overpressure in situ, several mechanisms have been suggested (Osborne and Swarbrick, 1997; Swarbrick et al., 2002). The overpressure may result from either (1) a reduction in the pore space, due to contraction of the solid matrix, or (2) an increase in the volume of pore fluid. In sedimentary basins and deltas, the main causes of matrix contraction are likely to be either vertical compaction during burial or horizontal contraction of tectonic origin. Amongst the mechanisms producing an increase in fluid volume are thermal dilation, mineralogical transformations (for example, smectite to illite) and hydrocarbon generation.

This last mechanism not only increases the volume of pore fluid, but also reduces that of the matrix. Probably the most efficient of all mechanisms is the production of thermogenic gas, which typically occurs at depths of over 5 km (Barker, 1990).

In a porous elastic material, fluid pressure can vary in space and time, in sympathy with the mean total stress (Shi and Wang, 1986; Ge and Garven, 1992; Neuzil, 1995):

$$\frac{k}{\nu_f} \nabla^2 P\Big|_{nh} + \alpha_b \frac{d\sigma_t}{dt} = \left[\phi\beta - \phi\beta_s + \alpha_b\right] \frac{dP}{dt} \tag{5}$$

Here $P|_{nh}$ is the non-hydrostatic part of the pore pressure (in other words, the overpressure or underpressure) that drives fluid flow, $\sigma_t$ is the mean total stress, $\alpha_b$ is the bulk compressibility, $\beta_s$ and $\beta$ express the compressibility of solid grains and pore fluid, respectively, and $Q$ is an internal source of fluid pressure (for example, by gas generation).

Eq. (5) is a generalized equation of diffusion. It expresses the fact that any fluctuation in fluid pressure has three potential contributions. One of them is the source term, $Q$. Another is the variation in mean stress resulting from compaction:

$$\frac{\alpha_b}{\phi\beta - \phi\beta_s + \alpha_b}\frac{d\sigma_t}{dt}$$

The third is the pressure gradient, which derives from Darcy's law and governs fluid flow:

$$\frac{k}{(\phi\beta - \phi\beta_s + \alpha_b)v_f}\nabla^2 P\Big|_{nh}$$

Typically, $\beta = 4\times10^{-10}\ Pa^{-1}$ for water and $\beta_s = 10^{-11}\ Pa^{-1}$ for solid grains. The bulk compressibility, $\alpha_b$, depends mainly on the solid matrix and ranges from $10^{-8}$ to $10^{-11}\ Pa^{-1}$ (Ge and Garven, 1992; Shi and Wang, 1986), depending on the state of compaction. As a first approximation, we shall neglect $\beta_s$ in comparison with $\alpha$, so that Eq. (5) becomes:

$$\frac{k}{v_f}\nabla^2 P\Big|_{nh} + \alpha\frac{d\sigma_t}{dt} = \left[\phi\beta + \alpha\right]\frac{dP}{dt} + Q \tag{6}$$

This equation is valid for elastic deformation. In nature, however, most deformation is non-elastic and irrecoverable. For large deformation, the compressibility, as measured on samples of sediment, is not necessarily representative of the overall behaviour. Neuzil (1986) has suggested using a higher compressibility to take this disparity into account. From Eq. (6), we can distinguish two time scales: one ($T_c$) for the build-up of pressure and the other ($T_d$) for its dissipation.

### 2.3. Build-up of overpressure by loading without drainage

If the load increases quickly (due, for example, to a rapid rate of sedimentation or to tectonic thickening) and the permeability is small enough, then $T_c \ll T_d$ and diffusion can be neglected, so that Eq. (6) becomes:

$$\frac{dP}{dt} = \frac{\alpha_b}{\left[\phi\beta + \alpha\right]}\frac{d\sigma_t}{dt} \tag{7}$$

Here we have assumed that the source, $Q$, is also negligible. For young and readily compactable sediment, $\alpha_b \gg \beta$, so that Eq. (7) integrates to:

$$\Delta P = \Delta\sigma_t \tag{8}$$

The scaling of this equation does not imply any strong relationship between values of compressibility for matrix and fluid. Model materials must simply satisfy:

$$\alpha_b \gg \beta \tag{9}$$

Young's modulus for loose and dense sands ranges between 10 and 50 MPa. Thus, the compressibility $\alpha_b$ is around $10^{-7}\ Pa^{-1}$ or less, if we assume irreversible deformation. Water as an experimental pore fluid satisfies condition (9), because $\beta = 4\times10^{-10}\ Pa^{-1}$. On the other hand, condition (9) does not hold for air, because $\beta = 10^{-5}\ Pa^{-1}$, so that, from Eq. (7), the change in fluid pressure will be no more than 1% of the change in stress, $\Delta\sigma_t$.

### 2.4. Dissipation of overpressure

Now consider that $\sigma_t$ is invariant. Eq. (6) becomes:

$$\frac{\partial P}{\partial t} = \frac{k}{(\alpha_b + \phi\beta)v_f}\nabla^2 P|_{nh} \tag{10}$$

We also assume that $Q$ vanishes and that $\alpha_b \gg \beta$.

Eq. (10) governs the dissipation of overpressure by a diffusion mechanism (Darcy flow). The reference time for this diffusion is:

$$t_o = \frac{v_o\chi_o L_o^2}{k_o} \tag{11}$$

Here, $\chi_o = (\alpha_{bo} + \phi\beta_o)$. The reference time increases with fluid viscosity, hydraulic resistivity ($1/k_o$) and compressibility. The time ratio is therefore:

$$\gamma_t = \gamma_v\gamma_L^2\gamma_\chi\gamma_k^{-1} \tag{12}$$

In their experiments, Cobbold et al. (2001) applied Darcy's law:

$$q_i = \frac{k}{v_f}\frac{\partial P}{\partial x_i}\Big|_{nh} \tag{13}$$

The time ratio deduced from this equation is slightly different:

$$\gamma_t = \gamma_v\gamma_L^2\gamma_\sigma^{-1}\gamma_k^{-1} \tag{14}$$

If the elastic properties of the material are properly scaled, we must have $\gamma_\sigma = \gamma_\chi^{-1}$ (Hubbert, 1937), so that Eqs. (12) and (14) become identical. In contrast, if the elastic properties of a model material are not properly scaled, as so often happens in practice (Ramberg, 1967), Eq. (12) may be preferable.

In the previous paragraph, we have demonstrated that water makes a good pore fluid for modelling the generation of overpressure by compaction. By assuming reference values of $k_m = 5\times10^{-11}\ m^2$ (Table 1), $k_r = 10^{-16}\ m^2$, $\alpha_{br} = 10^{-8}\ Pa^{-1}$, $\alpha_m = 10^{-7}\ Pa^{-1}$ and $\gamma_L = 10^{-5}$, the time ratio is $2\times10^{-15}$. This means that 1 s in an experiment is equivalent to 15 Ma in nature! The reference time for diffusion in a sand model, 3 cm thick, is close to 2 ms if the fluid is water and 1.5 ms if it is air.

Table 1
Permeability of model material, for different grain sizes

| Material | Grain size ($10^{-6}$ m) | Permeability ($10^{-12}\ m^2$) |
|---|---|---|
| Sand 1 | 315–400 | 120±10 |
| Sand 2 | 200–315 | 70±5 |
| Sand 3 | <200 | 30±5 |

This means that, although we can model the generation of fluid overpressures by a compaction mechanism when the material is very compressible, dissipation is quasi-instantaneous. Thus, properly scaled analogue modelling of such transitory phenomena, using air or water as a pore fluid and sand as a brittle material, would seem to be impossible. In addition, it may be difficult to model any changes in permeability during faulting.

In conclusion, our sand models will be scaled for the balance of forces, stresses and fluid pressures, but not for time. The fluid pressure distribution in the sand will be controlled only by the boundary conditions and transitory overpressures will be negligible. Water and air have different viscosities, but they can equally well be used. Nevertheless, for practical reasons, it may be easier to use air.

## 3. Stability of an infinitely long submarine slope with abnormal fluid pressures

By carrying part of the stress, a fluid overpressure reduces the frictional resistance within sloping sediments and can trigger gravitational gliding. To estimate slope stability, it is usually enough to consider variations in one dimension (Terzaghi, 1950; Hubbert and Rubey, 1959; Lambe and Whitman, 1969; Crans et al., 1980; Mandl and Crans, 1981; Mello and Pratson, 1999). The assumption is that the slope is infinitely long, so that longitudinal stress gradients are negligible. The gradient of fluid overpressure and the direction of fluid flow are assumed to be perpendicular to the slope. Mandl and Crans (1981) justified this approximation on the grounds that compaction is invariant along the slope and that the principal axes of the permeability tensor (which is potentially anisotropic) are approximately parallel and perpendicular to the free surface.

In terms of coordinates $x$ and $z$, parallel and perpendicular to the slope, Eq. (1) becomes:

$$\frac{\partial \sigma'_{xz}}{\partial z} = \rho_b g \sin\alpha - \frac{\partial P}{\partial x} \tag{15}$$

$$\frac{\partial \sigma'_{zz}}{\partial z} = \rho_b g \cos\alpha - \frac{\partial P}{\partial z} \tag{16}$$

If the sediment has a Mohr–Coulomb yield envelope, gliding will occur when the shear stress on a plane parallel to the slope reaches the yield stress:

$$\sigma'_{xz} = \tau_f = c + \mu\left(\sigma'_{zz} - P\right) \tag{17}$$

In stratified sediment, the pressure gradient varies from one layer to another, in response to changes in permeability (Fig. 2). The yield stress is reached at a depth $Z_d$ (Fig. 2), which is determined by the intensity of overpressure. At this depth, a detachment appears and the sediment begins to slide.

## 4. Experiments on gravity spreading

In a first series of experiments, we have used the apparatus of Cobbold et al. (2001) to model the development of normal faults and the propagation of a detachment during gravity spreading of a sedimentary sequence (Fig. 3). Each model was housed in a bottomless rectangular plastic box (30 cm long and 20 cm wide). The box rested on a reservoir for compressed air, which provided a uniform fluid pressure. A sieve at the base of the box allowed air to percolate into the overlying sand. Models were constructed in successive layers in order to create non-linear profiles of pore pressure, as in nature (Fig. 2). The bottom layer, 1 cm thick, was of coarse sand (315–400 μm). The next layer, 1 cm thick, was of fine sand (125–200 μm) and had a smaller permeability (Table 1). The third and final layer, 3 cm thick, was again of coarse sand. For such a multilayered model, pressure profiles are necessarily kink-like, if fluid migrates upwards (Fig. 3).

At the beginning of each experiment, the apparatus was tilted a few degrees. The end wall of the box was then withdrawn at a steady velocity of 10 cm/h. This allowed the model, except for its basal layer of coarse sand, to spread under its own weight. The displacement of the end wall was limited to 5 cm, except in experiments 7d and 11b, where it was stopped at 3.5 and 3.2 cm, respectively, because blowouts occurred at the upper end of the model (Fig. 4d and f).

To understand how the detachment was operating, we slightly improved on the experimental technique, by introducing into some experiments (7c and 11b) a series of coloured internal markers (Fig. 4). Transverse lines of coloured sand were built into (1) the basal coarse-grained layer and (2) the

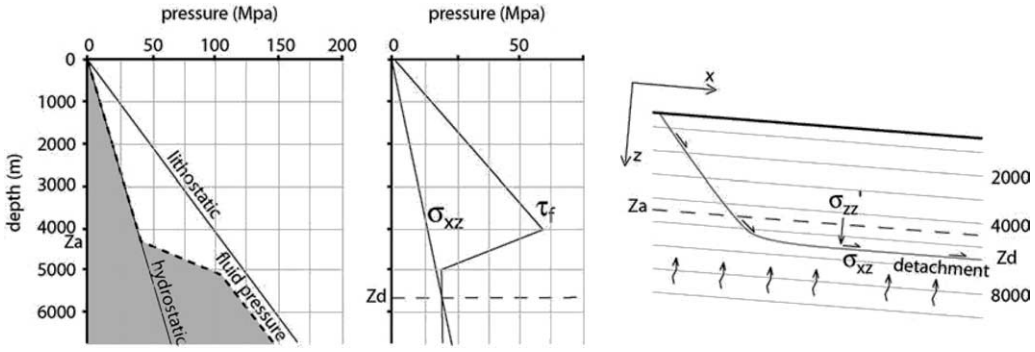


Fig. 2. One-dimensional analysis of slope stability. Above depth $Z_a$, pore fluid is in hydrostatic state (a). Beneath it, rapid increase in pore pressure results from confining layer of small permeability. Even further down, pore fluid maintains nearly lithostatic pressure. For an infinite slope, shear stress $\sigma_{xz}$ becomes equal to yield stress $\tau_f$ at depth $Z_d$ (b), triggering detachment (c).

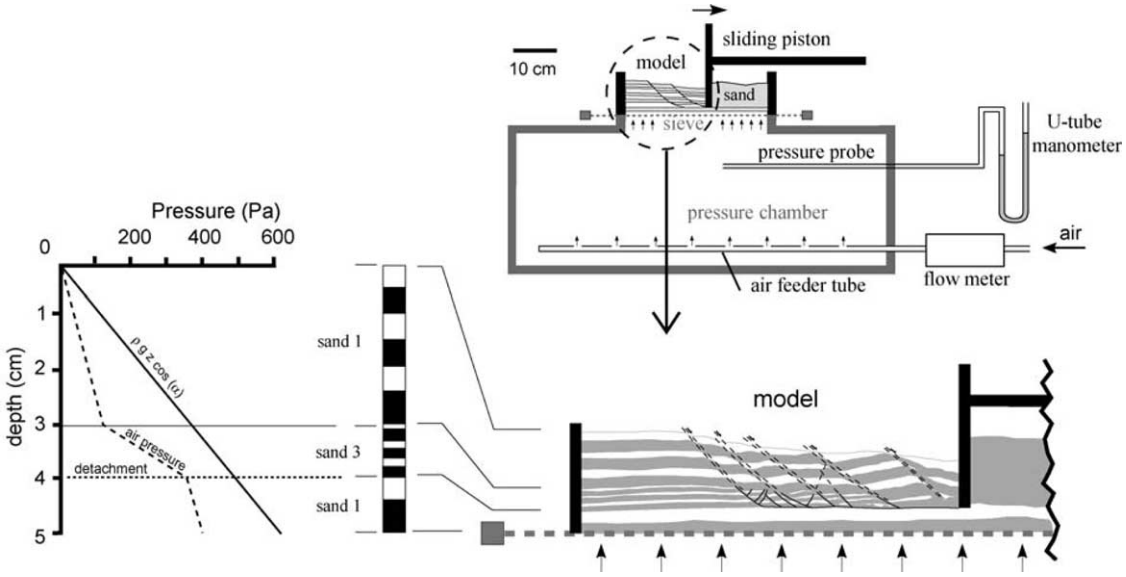


Fig. 3. (A) Apparatus for experiments on gravitational spreading. Model rests on sieve, which occupies window in pressure chamber. Compressed air enters pressure chamber through feeder tube and percolates through sieve and overlying model. Pressure is measured with U-tube manometer. Withdrawal of sliding piston allows model to spread under its own weight. (B) Details of multilayered model. Sand 1 and Sand 3 are described in Table 1. (C) Theoretical profiles of pressure in multilayered model. Fluid pressure approaches lithostatic values at base of fine sand (Sand 3).

overlying fine-grained layer. The markers were in pairs, vertically aligned. As a result of deformation, they became offset. We conducted two series of spreading experiments (series A and series B), for various values of basal fluid pressure. At the end of each experiment, we rendered the models cohesive, by wetting them, and then we sectioned them (Fig. 4).

### 4.1. Series A

The apparatus was tilted through 7° and experiments were done for basal fluid pressures ($P_b$) ranging from 0 to 620 Pa. For little or no fluid flow ($P_b < 300$ Pa), the models remained stable and no internal structures appeared. Instead, a natural talus formed in the space left behind by the moving end wall. The larger was the fluid pressure, the smaller was the slope of the talus. At intermediate values of fluid pressure, normal faults developed. For moderate pressures ($P_b = 300$ and 500; Fig. 4a and b), normal faults were numerous and closely spaced. Between them were rotated blocks. Deformation propagated from the sliding wall toward the back of the box. The rate of propagation was faster for higher pressures. Thus, at the end of experiment 7c, deformation had reached the back of the box (Fig. 4c). In this experiment, the final offsets of the coloured markers into the basal coarse-grained layer and the overlying fine-grained layer decreased systematically towards the back of the box, confirming that the overlying material had slid as a series of small blocks, separated by normal faults (Fig. 4c). At the highest values of fluid overpressure (experiment 7d) only three faults formed, bounding non-rotated rigid blocks (Fig. 4d). In the first stages of this experiment, faults formed at the back of the box. In all experiments, normal faults rooted into a detachment, beneath the layer of small permeability. The underlying coarse-grained layer never deformed.

For these experiments, we have measured the dip of the youngest normal fault and plotted it against the fluid pressure at the base of the model (Fig. 6). For values of $P_b$ between 400 and 550 Pa, faults flatten (from 57 to 50°) with increasing fluid pressure. For the highest pore fluid pressure (620 Pa; experiment 7d), the fault dip is much larger (close to 62°).

### 4.2. Series B

In these experiments, the apparatus was tilted through 11°. The results were basically similar to those of series A. For little fluid flow, models were stable. In experiment 11a ($P_b = 450$ Pa), faults were closely spaced, blocks rotated and deformation propagated towards the back (Fig. 4e). At higher fluid pressure ($P_b = 500$ Pa; experiment 11b), faults bounded non-rotated and rigid blocks (Fig. 4f). Coloured markers 5–7 acquired identical offsets of 2 cm, whereas markers 3 and 4 acquired smaller offsets (Fig. 4f). This result proves that the detachment was efficient and that the overlying sand slid essentially as two rigid blocks, separated by an extensional normal fault. The detachment appeared in the initial stages of the experiment and deformation reached the back of the box at the same time. There were, however, some differences between series A and series B. In series A, all faults had the same vergence, whereas in series B, a few antithetic faults formed. In contrast, Vendeville (1987) and McClay and Ellis (1987) reported that, for sand packs stretching above a rubber sheet, antithetic faults were more numerous when slopes were gentler.

### 4.3. Discussion

#### 4.3.1. Nature of the detachment

In the experiments of series A and series B, the style of deformation depended on the fluid pressure. For high fluid

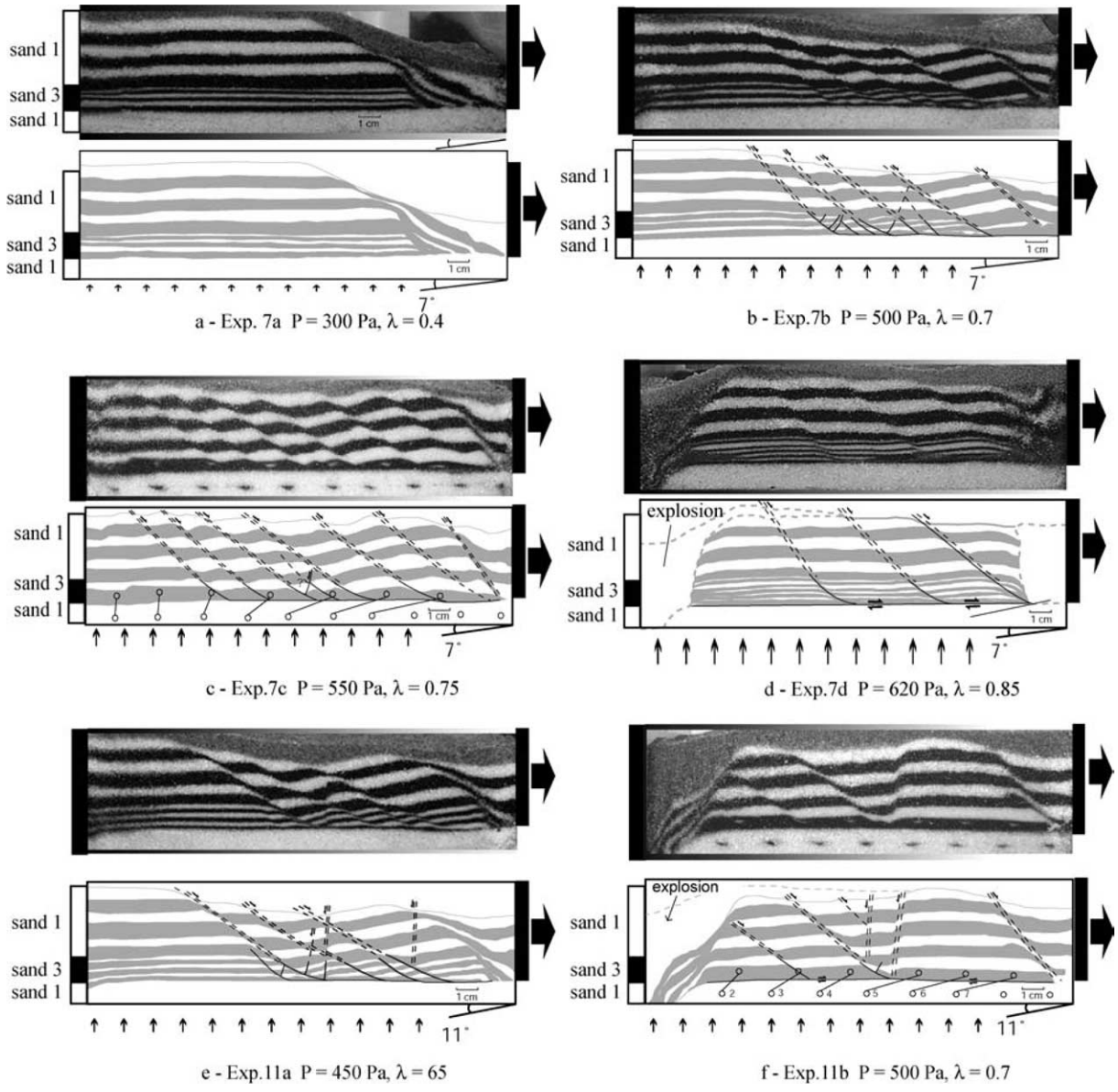


Fig. 4. Experiments on gravitational spreading. Photographs show final stages of deformation for longitudinal sections. Line drawings show interpretations. Models were built in three layers (made of Sand 1 or Sand 3). Models a–d (Series A) were tilted through 7°, models e and f (Series B) through 11°. Fluid pressure $P$ was measured at base of model and non-dimensional fluid pressure, $\lambda = P/(\rho g z \cos\alpha)$, was calculated for base of fine sand (Sand 3). In experiments 7c and 11b, markers (black or white diamonds in photographs) were introduced near base of sand. Before deformation, pairs of markers were vertically aligned. After deformation, markers (open circles, in interpretations) became offset (so that linking straight lines are now oblique).

pressure (experiments 7d and 11b), detachment was efficient and appeared in the initial stages of deformation. The overlying sand slid essentially as a series of rigid blocks. For lower fluid pressure (experiments 7c and 11a), deformation propagated from the sliding wall towards the back of the box and the overlying material slid as a series of smaller rotated blocks, separated by normal faults.

To understand how the detachment was operating, we can assume that the slope was infinitely long and estimate the shear stress $\sigma'_{xz}$ at the base of the fine sand in experiments 7c and 7d. Under these conditions, by integration of Eq. (15):

$$\sigma'_{xz} = \rho_b g z_d \sin\alpha - P_d \tag{18}$$

To a good approximation, the yield stress, $\tau_f$, on a plane parallel to the slope is given by the Mohr–Coulomb envelope (Eq. (4)). Because the sand was poured and not sifted, we take a smaller coefficient of internal friction ($\mu = 1$) than that determined by Mourgues and Cobbold (2003). We also assume that the cohesion is negligible. Under these conditions, for experiments 7c and 7d, the basal shear stress is smaller than the yield stress (Fig. 5). We can define a safety parameter, $F_{Saf} = \sigma'_{xz}/\tau_f$, at the base of the fine sand. For experiment 7c, $F_{Saf} = 0.5$, but for experiment 7d, $F_{Saf} = 0.85$. We infer that the second model was closer to failure, so that a detachment formed more easily. More realistically, the withdrawal of the end wall should have decreased the longitudinal stress $\sigma'_{xx}$ and

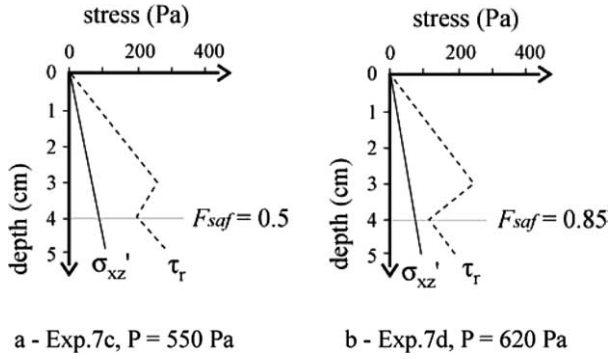


Fig. 5. Theoretical profiles of shear stress for two experiments (7c and 7d; Fig. 4). Shear stress $\sigma'_{xz}$ is for infinite slope and yield stress $\tau_f$ is for plane parallel to slope. Safety parameter $F_{Saf}$ is defined as $(\sigma'_{xz}/\tau_f)$.

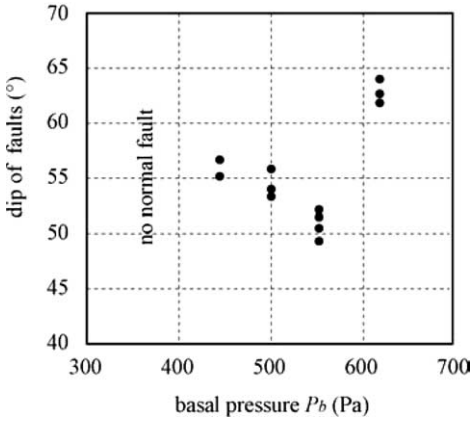


Fig. 6. Measured dip of normal faults versus basal fluid pressure, $P_b$, for models tilted through 7°.

therefore its gradient $\partial\sigma'_{xx}/\partial x$. From the equations of stress equilibrium (1), any such decrease must have been compensated by an increase in the vertical gradient of shear stress, $\partial\sigma'_{xz}/\partial z$. In experiments 7d and 11b, this change should have been enough for the basal shear stress to reach the yield stress, creating a detachment throughout the model.

### 4.3.2. Dips of normal faults

In the experiments of series A, we observed that the dip of the youngest faults depended on the fluid pressure (Fig. 6). The same remark can be made for the experiments of series B. For values of $P_b$ between 400 and 550 Pa, we attribute the flattening of the faults to seepage forces (Mourgues and Cobbold, 2003). The equations of state for effective stress (1) can be written:

$$\frac{\partial\sigma'_{ij}}{\partial x_j} = (1-\phi)(\rho_s-\rho_w)g_i - \frac{\partial P}{\partial x_i}\Big|_{nh} \tag{19}$$

Here $\phi$ is porosity, $\rho_s$ and $\rho_w$ are solid and water density, respectively, and the composite subscript nh refers to the non-hydrostatic part of the fluid pressure gradient. According to these equations, the forces acting on each element of solid matrix are (1) its weight $F_w=(1-\phi)\rho_s g$, (2) a buoyancy force, $F_a=-(1-\phi)\rho_w g$ and (3) a seepage force, $F_s=-\nabla P|_{nh}$. Although the first two forces act vertically, the third one may act in another orientation, so modifying the principal values and orientations of effective stresses. In our experiments, the seepage force was perpendicular to the slope. If conjugate faults develop above a velocity discontinuity, Mourgues and Cobbold (2003) have shown that principal stresses and faults flatten with depth, as a function of the increasing overpressure gradient (Fig. 7). For the highest fluid pressure (620 Pa), we

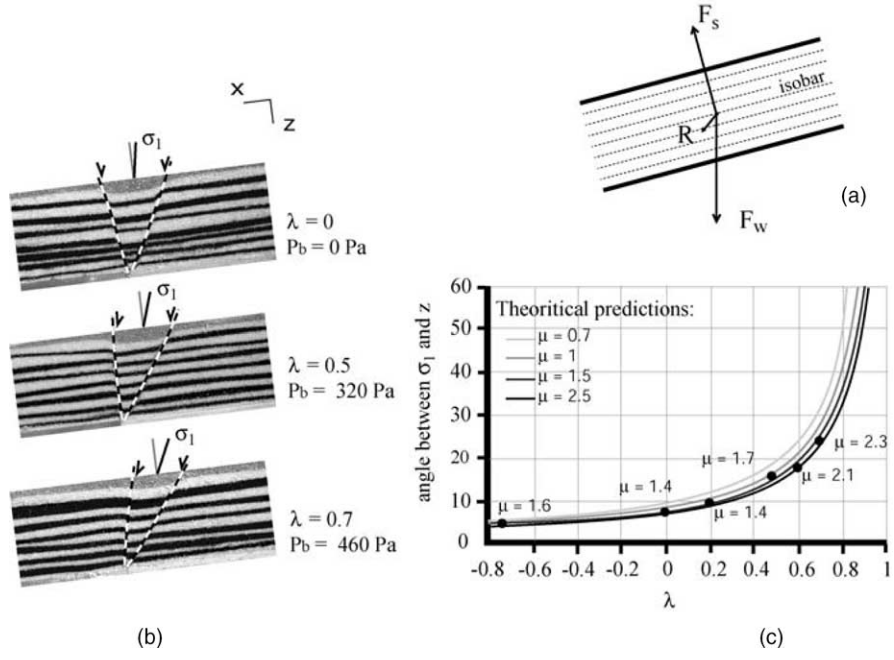


Fig. 7. Reorientation of principal stresses and conjugate extensional faults as function of overpressure gradient (after Mourgues and Cobbold, 2003). Conjugate extensional faults form above velocity discontinuity between sliding sieves (b). Assuming that maximal compressive stress $\sigma_1$ bisects dihedral angle between conjugate faults, angle between $\sigma_1$ and $z$ must increase with increasing ratio, $\lambda$. Theoretical curves are for infinite slope (c). Reorientation is due to seepage force $F_s$ (a).

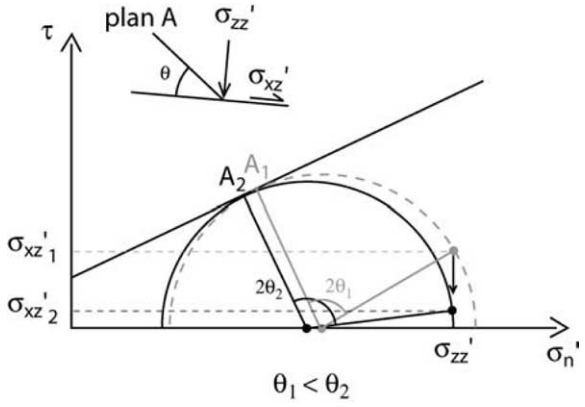


Fig. 8. Mohr diagram illustrating how a decrease in shearing resistance on a detachment causes normal faults to become steeper.

attribute the much larger fault dip to a decrease in shear stress on the detachment, as a result of softening during ongoing sliding. Such an effect has been observed in shear tests (Mandl et al., 1977). Assuming that the decrease is passed on into the upper part of the model and that $\sigma'_{zz}$ remains constant, we predict, from a Mohr circle for stresses at yield, that normal faults should be steeper (Fig. 8).

## 5. Experiments on gravity gliding

### 5.1. New apparatus with fluid injectors

At the scale of a continental slope or a delta, gravitational instability may result in a large sliding sheet. At its leading edge, there may be a belt of compressional deformation (fold-and-thrust belt).

It would appear that to model a sliding sheet of reasonable thickness requires a larger apparatus than the one described previously (20 cm by 30 cm). Moreover, in the previous experiments 7d and 11b, the displacement of the end wall was stopped before the end of the experiment, because blowouts occurred at the upper end of the model (Fig. 4d and f). These devastating explosions were due to a lack of overburden in the extensional part. To avoid such unstable explosions in experiments with high fluid pressures, we needed to change the basal boundary conditions on pressure (constant pressure). So we constructed new apparatus, which allows us (1) to house larger models, (2) to vary the size and shape of the area of injection, (3) to control the fluid pressure at all points under the model and (4) to avoid devastating explosions.

As before, the new apparatus has a reservoir at uniform pressure (Fig. 9). This reservoir receives compressed air through a basal system of perforated plates, which diffuses the flow. From the reservoir, air flows through a first sieve and into a series of rectangular tubes (injectors), 5 cm wide. The model itself rests on a second sieve, immediately above the injectors. There are two ways of using the injectors (Fig. 10):

1. Each tube contains a different preset thickness of sand (Fig. 10a). The pressure in each tube depends on the thickness of sand within it and also on the thickness and permeability of overlying parts of the model. By selecting the thickness of sand in each tube, it is possible to approach a desired distribution of fluid pressure beneath the model, while the pressure in the reservoir remains constant.
2. Each tube is full of sand to the maximum height (25 cm). The tubes then act as buffers, regulating the flow of air between reservoir and model. Where the model is thin, the fluid pressure at the base is low; where the model is thick, the pressure is high (Fig. 10b). In other words, the ratio between pore pressure and overburden pressure is nearly constant. As a result of such buffering, explosions are less catastrophic or do not occur at all. This is the method that we have selected for the experiments that are described below.

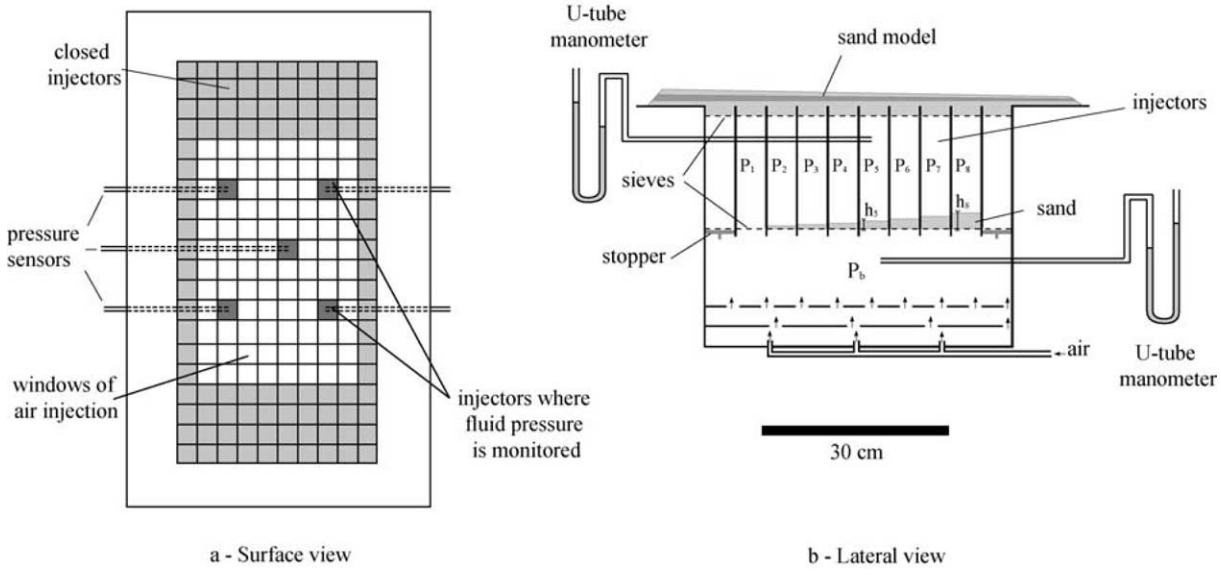


Fig. 9. New experimental apparatus. For detailed description, see text.

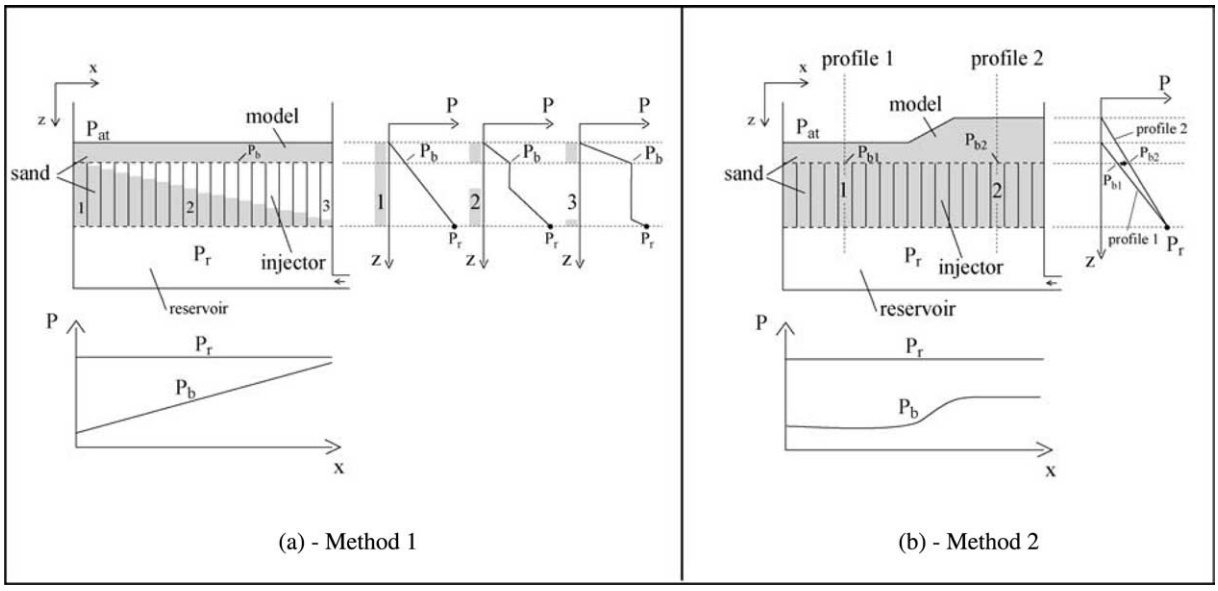


Fig. 10. Two methods of using injectors. In Method 1 (a), each tube contains different preset thicknesses of sand. Resulting pressure, $P_b$, at base of model varies horizontally. In Method 2 (b), all tubes are full of sand. They act as buffers, regulating flow of air between reservoir and model. Fluid pressure beneath model varies horizontally, in such a way that ratio $\lambda$ of pore pressure and overburden stress is nearly uniform, from one vertical profile to another.

An additional advantage of the new apparatus is that we may define a basal window of any required size or shape, simply by blocking the outlying tubes.

### 5.2. Fluidisation of fine sand at high fluid pressure

To test the new apparatus, we did an experiment at high fluid pressure. The aim was to trigger gravity gliding on a gentle slope. The injection window was 40 cm long by 25 cm wide (Fig. 11). On each side of the window and at its lower edge were walls of glass, which reduced the sliding friction. The internal structure of the model was similar to those described previously: 1 cm of coarse sand for the lowermost layer, 1 cm of fine sand for the intermediate one and 1.5 cm of coarse sand for the uppermost layer. Once the model was in place, we tilted the apparatus through 5° and increased the fluid pressure in the reservoir. At an estimated basal pressure of 450 Pa, the model started to slide. However, as a result of frictional stick-slip, the sliding soon stopped. We therefore increased the fluid pressure to 470 Pa and this produced further sliding. Rifts appeared near the trailing edge of the slide. At this stage, small bubbles reached the surface in the rifts, creating pockmarks, and fine sand from the intermediate layer spread out like a fluid on the free surface of the model.

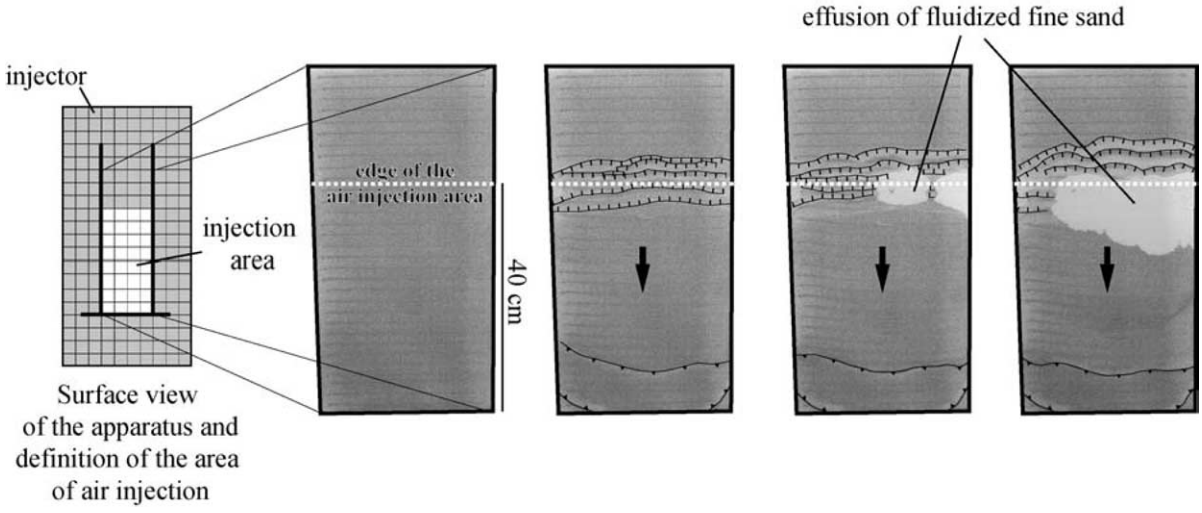


Fig. 11. Four stages in the progressive development of surface structures during gravitational gliding. Model and new apparatus were tilted through 5°. Gliding (black arrows) occurred when fluid pressure reached critical value. It resulted in rifts at trailing edge of gliding sheet and thrusts at leading edge. In contrast to what happened using the previous apparatus, no devastating explosions occurred in rifts. Instead, small bubbles reached the surface and sheet of fluidised sand, coming from the intermediate layer, and spread out on the surface.

In contrast to what happened in previous experiments on gravity spreading, the fluidisation was stable and did not degenerate into devastating explosions.

### 5.3. Length of detachment and dynamics of sliding

To test the dynamics of gliding and to calibrate future experiments, we did a series of experiments using injection windows of various lengths. The configurations of the models were similar to those described in the previous section. The sliding mass was 2.5 cm thick. The injection windows were 20, 30, 50 or 70 cm long. The window was 20 cm from the lower endwall. We increased the pressure in the reservoir until the pressure at the base of the model reached 400 Pa. Then we carefully and progressively tilted the apparatus, to a maximal slope of 18°, using a forklift truck and avoiding tremors. We took a photograph of the upper surface for every 0.2° of increasing slope.

In all experiments, an extensional domain appeared at the upper edge of the injection window (Fig. 12). In experiments Gl20 and Gl30, a single fore-thrust developed at the lower edge of the window. In experiments Gl50 and Gl70, three and four pop-ups appeared, bounded by fore-thrusts and back-thrusts. The first fore-thrust appeared at the lower edge of the window and the following ones stepped back, reducing the length of the rigidly gliding mass, as the slope increased. For each experiment, we plotted the displacement of a selected surface marker (star; Fig. 12) versus the angle of slope, obtaining the following results (Fig. 13a):

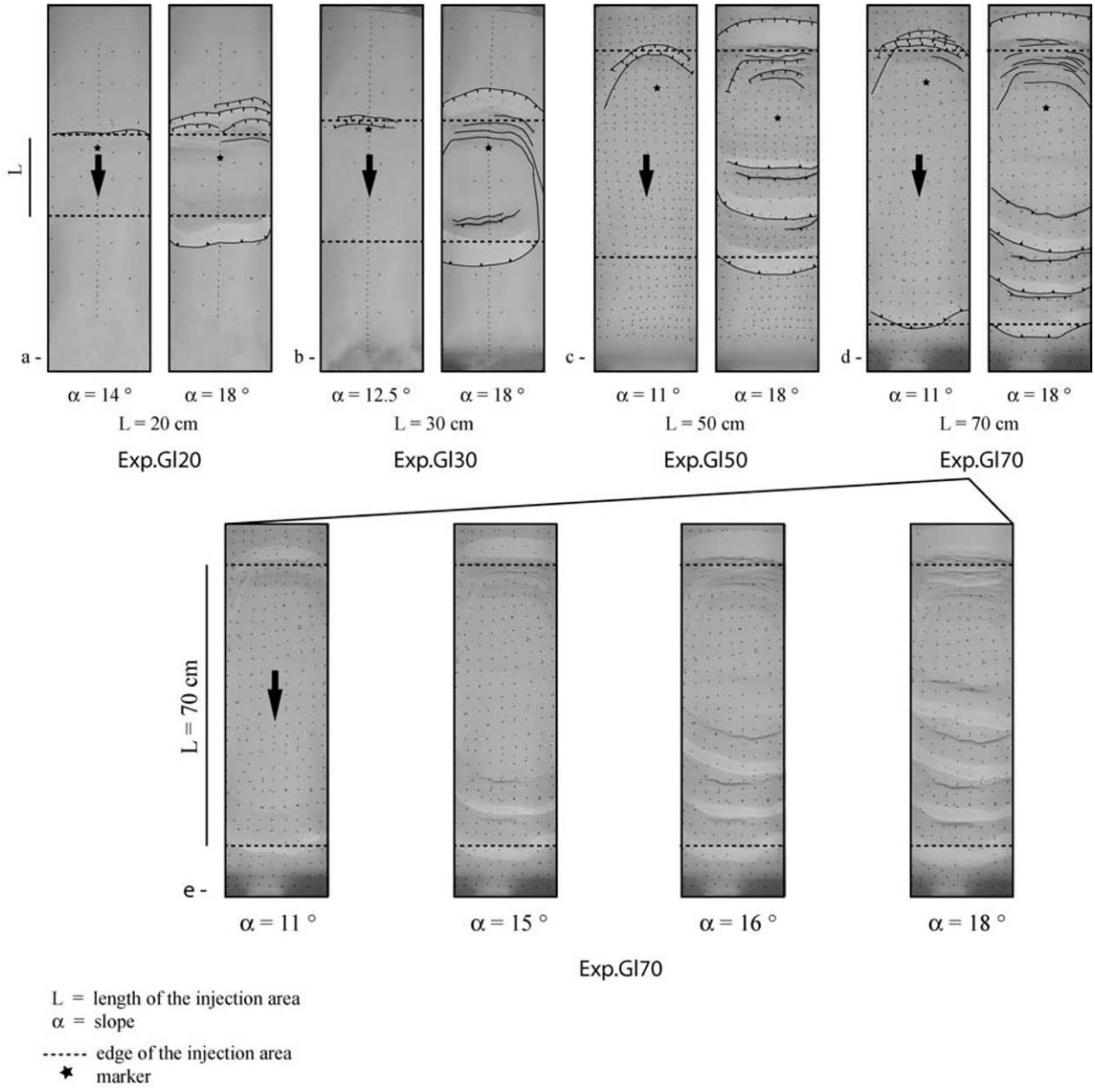


Fig. 12. Four experiments on gravitational gliding in the new apparatus. Length ($L$) of injection window varied, from one experiment to another. Photographs of upper surface show structural development, for increasing angles of slope ($\alpha$). Thrusts (traces lined by black triangles) formed sequentially, migrating upslope. For displacement history of marker (star), see Fig. 13.

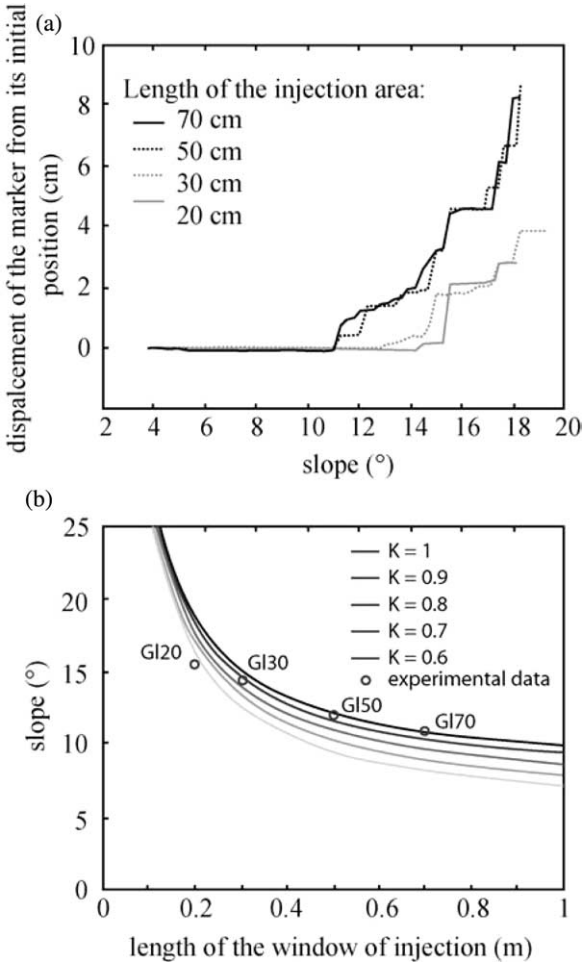


Fig. 13. (a) Displacement of a marker at the back of a sliding sheet versus angle of slope, for different lengths of injection window. For photographs of experiments and position of marker (star), see Fig. 12. (b) Comparison of experimental critical slope and analytical results.

1. The shorter was the injection window (and hence the slide), the steeper was the critical slope required for gliding to start. For models GL70 and GL50, the critical slope was 11 or 12°, whereas for models GL30 and GL20, it was more like 14 or 15°.
2. Displacement accumulated in steps.
3. The magnitude of the first step was proportional to the length of the slide. For model GL70, the first step was 1 cm long. This was enough to develop a fore-thrust at the leading edge (Fig. 12d). For model GL50, the first step was more like 0.5 cm and no thrust fault developed. For models GL20 and GL30, the markers moved progressively and extensional structures appeared at the upper edge of the injection window; but true sliding did not occur until the slope had reached about 15° (the critical slope).
4. Each step, or sudden increase in displacement, correlated with the development of a fore-thrust or pop-up. During the intervening periods of stability, no structures were developing.
5. In our experiments, compressional failure occurred within the injection window, but not outside it. As a result, successive thrusting could only propagate upslope and the length of the rigidly gliding sheet necessarily decreased. However, it never became shorter than 20 cm. By then, the slope was about 15°. At later stages, all sheets appeared to behave in much the same way. Steps were as large as 2 cm and they alternated with periods of stability, during which the slope increased by as much as 2°.

### 5.4. Discussion

#### 5.4.1. Analytical model of gravity gliding

When a detachment appears in sloping sediments, part of the weight is taken off the base and thrown against the toe of the slope. In terms of stress gradients, ($\sigma_{xz}$/($z$ diminishes and ($\sigma_{xx}$/($x$ increases (Eq. (1)). If the slope is long enough, the increase in $\sigma_{xx}$ leads to failure, by development of thrust faults at the toe of the slope. For a given angle of slope, Mandl (1988, p. 212) determined the maximal length of an infinitely wide sheet, by assuming that the stress gradient ($\sigma_{xx}$/($x$ results from a decrease in sliding resistance on the basal detachment. Alternatively, for a given length of slide, the slope must be wide enough for the unbalanced weight to overcome the resistance at the toe, creating thrust faults. In a slide of finite width, the stress gradient ($\sigma_{xx}$/($x$ also depends on the frictional resistance at the lateral edges of the slide, that is to say on its width, and the resistance at the toe is controlled by the presence of fluid overpressure in the sliding sheet.

To quantify these parameters and to explain the results of our experiments on gravity gliding, we have developed a quasi-3D analytical model of a sliding sheet with lateral friction (Fig. 14 and Appendix A). It is based on the following assumptions. (1) The sliding sheet is bounded by a normal fault at the trailing edge and by a thrust fault at the leading edge. (2) The sheet slides on a basal detachment (at a depth $H$) that is parallel to its upper surface. (3) There is lateral friction, but $\sigma'_{xy}$ and $\sigma'_{xx}$ are constant in the $y$ direction. (4) At yield, effective stresses satisfy a Coulomb criterion. (5) Fluid pressure on the detachment ($\lambda_b$) is different from that in the body of the sheet ($\lambda$). (6) Gliding occurs when the yield stress is reached at the leading edge.

We have plotted some solutions of the analytical model (Fig. 15) to show how the critical slope depends on (1) the length of the slide, (2) lateral friction and the width of the sheet, and (3) fluid pressure. For a sheet longer than 1 m ($L/H > 30$), the critical slope is only a few degrees more than for an infinitely long model (Fig. 15a and b). For a shorter sheet, the resistance to sliding is significant. It becomes a first-order

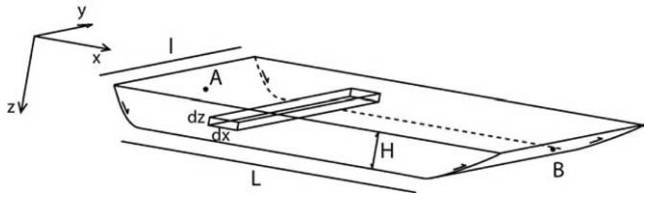


Fig. 14. Configuration of analytical model (Appendix A).

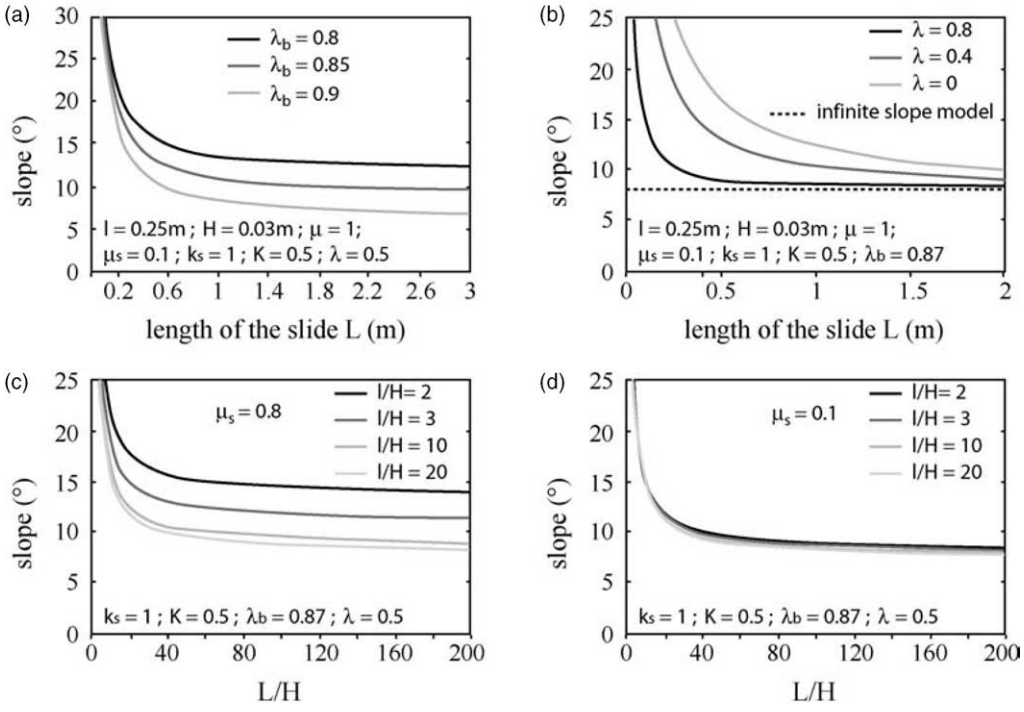


Fig. 15. Results of analytical model (Appendix A). (a) Critical slope for sliding, as function of length of sliding sheet ($L$), for various values of basal fluid pressure, $\lambda_b$. (b) The same, but for internal fluid pressure, $\lambda$. (c) and (d) Effect of lateral friction.

parameter for sheets shorter than 60 cm ($L/H<20$). Lateral friction also contributes to the sliding resistance (Fig. 15c and d). The slope required to trigger a slide increases as its width diminishes. For wide sliding sheets ($L/H>20$), lateral friction is negligible.

The final parameter that controls the resistance to sliding is the strength of the sheet. This depends on the material, but also on the fluid overpressure. We distinguish between pressure at the base of the sheet and pressure within it. For both factors, overpressure reduces the critical slope for sliding, but for different reasons. For long sheets, the basal pressure is more important (Fig. 15a), because it reduces the resistance to sliding. For short sheets, the internal pressure is more important (Fig. 15b), because it decreases the resistance of thrust faults at the leading edge.

### 5.4.2. Analysis of experimental results

The first result of the experiments on gliding was that the shorter was the injection window, the steeper was the critical slope required for gliding to start. This seems to be in agreement with theory. Fig. 13b shows that our analytical model provides good predictions of this experimental result. The second result was that the magnitude of the first step was proportional to the length of the slide. For models with a long detachment (model GL70), the first step was 1 cm long and went with the development of a fore-thrust at the leading edge. For the smallest models (GL20 and GL30), the sand moved progressively before true sliding occurred. In this case, we attribute the first displacements to longitudinal compaction within the sliding sheet, which otherwise remained stable, because of resistance at the leading edge. Nevertheless, the basal detachment must have been already active. Indeed, for models GL20 and GL30, the observed critical slopes fit the curves for lower basal friction (that is, a coefficient of softening $k_s<1$; see Appendix A); whereas, for models GL50 and GL70, the observed critical slopes fit the curves for higher basal friction (Fig. 13b). We infer that detachment was active before the critical slope was attained and that this preliminary activation resulted in softening on the detachment.

Finally, the step-like displacement curves (Fig. 13) are partly due to the sequential nature of the thrusting, in response to fluctuations in the longitudinal stress. Nieuwland et al. (2000), using sensitive strain gauges, have measured such fluctuations, in experiments on thrusting in sand packs. As soon as one thrust has formed, the resistance to slip on it decreases, leading to a period of rapid slip. However, slip on that thrust results in local thickening of the model, which in turn causes an increase in resistance to slip. A period of stability then ensues, during which the longitudinal stress builds up again, to the failure limit. At that point, another thrust forms and the process repeats. Although a similar process should occur in models that detach on a ductile layer, we would not predict for them such sudden increases in displacement, but rather more gentle increases. Notice also that in our experiments, the sudden increases in displacement may have meant that significant inertial forces were involved. If so, Eq. (1) needs additional terms.

## 6. Conclusions

We have used a relatively new technique (injection of compressed air into sand packs; Cobbold et al., 2001) to model the triggering of gravitational instabilities by fluid

overpressure. Basal detachments take the appearance of thin flat shear bands, in contrast to what happens in experiments where silicone putty provides the basal weakness. In experiments on gravity spreading, fluid overpressure facilitated detachment and extensional deformation. At moderate values of fluid overpressures, normal faults propagated upslope, from the leading edge to the trailing edge of the sliding sheet. Numerous closely spaced normal faults formed between quasi-rigid blocks that tilted. At the highest overpressures, the deformation propagated very fast and blocks slid without tilting on an efficient basal detachment. The angle of fault dip was a function of fluid pressure and of frictional resistance at the base. To model gravitational gliding, we have built a new apparatus with injectors, which allows us to change the shape of the overpressured window and which avoids devastating explosions. We have carried out a series of experiments using injection windows of various lengths. In models shorter than 60 cm, frictional resistance at the leading edge controlled the dynamics of gliding and the critical slope that was necessary to trigger the slide. Gliding occurred in steps, during which sudden increases in displacement alternated with periods of stability, due to the sequential nature of thrusting at the leading edge. The experimental results agree with analytical predictions.

These experiments represent a first stage in the analogue modelling of gravitational instabilities due to overpressures on delta slopes and passive margins. They pave the way for more realistic models of tectonics involving non-viscous detachments. In a future article, we aim to model more realistic geometries of delta slopes, as well as spatial variations of overpressures and sedimentation. Nevertheless, readers should be aware of one major limitation of the technique: transitory phenomena (overpressure build-up or dissipation) are not scaled but imposed by the experimenter. Also, it may be difficult to model any change in permeability during faulting.

## Acknowledgements

The authors wish to thank F. Storti and B. Vendeville for their constructive reviews.

## Appendix A. Analytical model of a sliding sheet in three dimensions

We consider a sliding sheet in three dimensions (Fig. 14). The sheet abuts a normal fault at its trailing edge and a thrust fault at its leading edge. At a depth $H$, the sheet slides on a basal detachment, which is parallel to the upper surface of slope $\alpha$. We consider lateral friction but we assume that $\sigma'_{xy}$ and $\sigma'_{xx}$ are constant in the $y$ direction. For an elementary volume d$V$ of thickness d$z$, length d$x$ and width $l$ (width of the slide), at depth $H/2$, we write the balance of forces, making four further assumptions.

1. For lateral friction, we assume a Coulomb criterion, where $\mu_s$ is the coefficient of sidewall friction.
2. Following the silo model (Jansen, 1895; Mourgues and Cobbold, 2003), we assume that the vertical stress $\sigma'_v$ automatically results in a proportional horizontal stress $\sigma'_h$:

$$\sigma'_h = K\sigma'_v \tag{A1}$$

This assumption is valid for granular or elastic media. In granular materials, 0.5 is a suitable value for $K$ (Lambe and Whitman, 1969), so that:

$$\sigma'_{yy} = K(\rho gz/\cos\alpha - P) \tag{A2}$$

3. For basal friction on the detachment, we also assume a Coulomb criterion and we introduce the parameter $k_s$ that represents softening on the shear zone. At depth $H$:

$$\sigma'_{xz} = k_s\mu\sigma'_{zz} \tag{A3}$$

At yield, $k_s = 1$ and after activation of the detachment $k_s$ diminishes.

4. We assume a linear variation of $\sigma'_{xz}$ with depth between surface and detachment.

We now write the balance of forces across the volume d$V$ in the $x$ direction, using Eqs. (A1)–(A3):

$$\mathrm{d}\sigma'_{xx}\mathrm{d}zl + 2\mu_s K\left(\frac{\rho gH}{2\cos\alpha} - P\Big|_{z=H/2}\right)\mathrm{d}x\mathrm{d}z + k_s\mu(\rho g\cos\alpha - P\Big|_{z=H}/H)\mathrm{d}x\mathrm{d}zl = \rho g\mathrm{d}x\mathrm{d}zl\sin\alpha \tag{A4}$$

On simplifying, we obtain:

$$\mathrm{d}\sigma'_{xx} = \rho g\mathrm{d}x\sin\alpha - 2\mu_s K\left(\frac{\rho gH}{2\cos\alpha} - P\Big|_{z=H/2}\right)\frac{\mathrm{d}x}{l} - k_s\mu\left(\rho g\cos\alpha - P\Big|\frac{z=H}{H}\right)\mathrm{d}x \tag{A5}$$

At the trailing and leading edges of the sheet, on normal and thrust faults, we assume that stresses are at yield. At a depth $H/2$, we estimate $\sigma'_{zz}$ and $\sigma'_{xz}$ to be:

$$\sigma'_{zz} = \rho g(H/2)\cos\alpha - P\Big|_{z=H/2}$$

$$\sigma'_{xz} = k_s\mu(H/2)\left(\rho g\cos\alpha - P\Big|_{z=H}/H\right)$$

From these values, we determine $\sigma'_{xx}$ at yield in the extensional and compressional parts of the sheet and we deduce the total variation of $\sigma'_{xx}$ ($\Delta\sigma'_{xx}$) in the sliding sheet (Fig. A1),

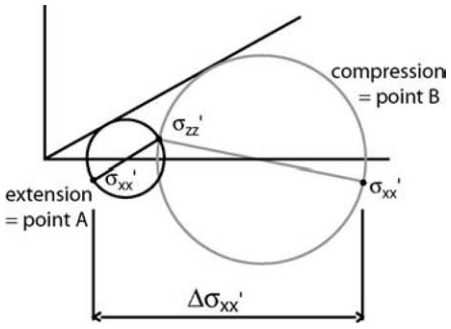


Fig. A1. Mohr circles for states of stress at compressional leading edge and extensional trailing edge of gliding sheet, according to analytical model. For further explanation, see text.

between points A and B (Fig. 14). Then, from Eq. (A5), we obtain the length of the sheet *L*.

## References


Barker, C., 1990. Calculated volume and pressure changes during the thermal cracking of oil to gas in reservoirs. American Association of Petroleum Geologists Bulletin 74, 1254–1261.

Brun, J.P., Choukroune, P., 1983. Normal faulting, block tilting and decollement in a stretched crust. Tectonics 2, 345–356.

Brun, J.P., Fort, X., 2004. Compressional salt tectonics (Angolan margin). Tectonophysics 382, 129–150.

Byerlee, J.D., 1978. Friction of rocks. Pure and Applied Geophysics 116, 615–626.

Cobbold, P.R., Castro, L., 1999. Fluid pressure and effective stress in sandbox models. Tectonophysics 301, 1–19.

Cobbold, P.R., Szatmari, P., 1991. Radial gravitational gliding on passive margins. Tectonophysics 188, 249–289.

Cobbold, P.R., Durand, S., Mourgues, R., 2001. Sandbox modelling of thrust wedges with fluid-assisted detachments. Tectonophysics 334, 245–258.

Cobbold, P.R., Mourgues, R., Boyd, K., 2004. Mechanism of thin-skinned detachment in the Amazon Fan: assessing the importance of fluid overpressure and hydrocarbon generation. Marine and Petroleum Geology 21, 1013–1025.

Cohen, H.A., McClay, K., 1996. Sedimentation and shale tectonics of the northwestern Niger Delta front. Marine and Petroleum Geology 13, 313–328.

Crans, W., Mandl, G., Haremboure, J., 1980. On the theory of growth faulting: a geomechanical delta model based on gravity sliding. Journal of Petroleum Geology 2, 265–307.

Dahlen, F.A., 1990. Critical taper model of fold-and-thrust belts and accretionary wedges. Annual Review of Earth and Planetary Sciences 18, 55–99.

Damuth, J.E., 1994. Neogene gravity tectonics and depositional processes on the deep Niger Delta continental margin. Marine and Petroleum Geology 11, 320–346.

Davy, P., Cobbold, P.R., 1991. Experiments on shortening of a 4-layer model of the continental lithosphere. Tectonophysics 188, 1–25.

Evamy, B.D., Haremboure, J., Kamerling, P., Knaap, W.A., Molloy, F.A., Rowlands, P.H., 1978. Hydrocarbon habitat of Tertiary Niger Delta. American Association of Petroleum Geologists Bulletin 62, 1–39.

Fort, X., 2002. Processus de la tectonique salifère de la marge angolaise. PhD Thesis, University of Rennes 1, 225pp.

Ge, S., Garven, G., 1992. Hydromechanical modeling of tectonically driven groundwater flow with application to the Arkoma foreland basin. Journal of Geophysical Research 97 (B6), 9119–9144.

Hubbert, M.K., 1937. Theory of scale models as applied to the study of geologic structures. Geological Society of America Bulletin 48, 1459–1520.

Hubbert, M.K., Rubey, W.W., 1959. Role of fluid pressure in mechanics of overthrust faulting. Geological Society of America Bulletin 70, 115–166.

Jansen, H.A., 1895. Versuche über Getreidedruck in Silozellen. Zeitschrift des Vereiner Deutscher Ingenieure 39, 1045–1049.

Lambe, T.W., Whitman, R.V., 1969. Soil Mechanics. Wiley, New York. 553pp.

Maillard, A., Gaullier, V., Vendeville, B.C., Odonne, F., 2003. Influence of differential compaction on salt tectonics in Ligurian–Provençal Basin, Northwest Mediterranean. Marine and Petroleum Geology 20, 13–27.

Mandl, G., 1988. Mechanics of Tectonic Faulting: Models and Basic Concepts, Developments in Structural Geology. Elsevier, Amsterdam. 407pp.

Mandl, G., Crans, W., 1981. Gravitational gliding in deltas. In: McClay, K.R., Price, N.J. (Eds.), Thrust and Nappe Tectonics Geological Society of London Special Publication 9, pp. 41–54.

Mandl, G., de Jong, L.N.J., Maltha, A., 1977. Shear zones in granular material. Rock Mechanics 9, 95–144.

Mauduit, T., 1998. Déformation gravitaire synsédimentaire sur une marge passive: modélisation analogique et application au Golfe de Guinée. Mémoires de Géosciences-Rennes 83, 1–251.

Mauduit, T., Gaullier, V., Brun, J.P., Guerin, G., 1997a. On the asymmetry of turtle-back growth anticlines. Marine and Petroleum Geology 14, 763–771.

Mauduit, T., Guerin, G., Brun, J.P., Lecanu, H., 1997b. Raft tectonics: the effects of basal slope angle and sedimentation rate on progressive extension. Journal of Structural Geology 19, 1219–1230.

McClay, K., Ellis, P.G., 1987. Geometries of extensional fault systems developed in model experiments. Geology 15, 341–344.

Mello, U.T., Pratson, L.F., 1999. Regional slope stability and slope-failure mechanics from the two-dimensional state of stress in an infinite slope. Marine Geology 154, 339–356.

Morley, C.K., Guerin, G., 1996. Comparison of gravity-driven deformation styles and behavior associated with mobile shales and salt. Tectonics 15, 1154–1170.

Mourgues, R., Cobbold, P.R., 2003. Some tectonic consequences of fluid overpressures and seepage forces as demonstrated by sandbox modelling. Tectonophysics 376, 75–97.

Neuzil, C.E., 1986. Groundwater flow in low-permeability environments. Water Resources Research 22, 1163–1195.

Neuzil, C.E., 1994. How permeable are clays and shales? Water Resources Research 30, 145–150.

Neuzil, C.E., 1995. Abnormal pressures as hydrodynamic phenomena. American Journal of Science 295, 742–786.

Osborne, M.J., Swarbrick, R.E., 1997. Mechanisms for generating overpressure in sedimentary basins: a reevaluation. American Association of Petroleum Geologists Bulletin 81, 1023–1041.

Nieuwland, D.A., Urai, J.L., Knoop, M., 2000. In-situ stress measurements in model experiments of tectonic faulting. In: Lehner, F.K., Urai, J.L. (Eds.), Aspects of Tectonic Faulting. Springer, Berlin, pp. 155–166.

Ramberg, H., 1967. Model experimentation of the effect of gravity on tectonic processes. Geophysical Journal of the Royal Astronomical Society 14, 307–329.

Shi, Y., Wang, C.Y., 1986. Pore pressure generation in sedimentary basins: overloading versus aquathermal. Journal of Geophysical Research 91 (B2), 2153–2162.

Strayer, L.M., Hudleston, P.J., Lorig, L.J., 2001. A numerical model of deformation and fluid-flow in evolving thrust wedge. Tectonophysics 335, 121–145.

Swarbrick, R.E., Osborne, M.J., Yardley, G.S., 2002. The magnitude of overpressure from the main generating mechanisms under realistic basin conditions. American Association of Petroleum Geologists Memoir 76, 1–12.

Terzaghi, K.v., 1923. Die Berechnung der Durchlässigkeitsziffer des Tones aus dem Verlauf der hydrodynamischen Spannungerscheinungen. Sitzungsberichte der Akademie der Wissenschaften in Wien, mathematischnaturwissenshaftliche Klasse, Abteilung IIa 132, 125–138.

Terzaghi, K.v., 1950. Mechanics of landslides. In: Paige, S. (Ed.), Application of Geology to Engineering Practice. Geological Society of America, New York, pp. 83–123.

Vendeville, B., 1987. Champs de failles et tectonique en extension. Modélisation expérimentale. Mémoires et Documents du Centre Armoricain d'Etude Structurale des Socles 15, 1–395.

Vendeville, B., Cobbold, P.R., 1987. Glissements gravitaires synsédimentaires et failles normales listriques: modèles expérimentaux. Comptes Rendus de l'Académie des Sciences de Paris, Tome 305, Séries II 16, 1313–1320.

Worral, D.M., Snelson, S., 1989. Evolution of the northern Gulf of Mexico, with emphasis on Cenzoic growth faulting and the role of salt. In: Bally, A.W., Palmer, A.R. (Eds.), The Geology of North America: an Overview Geological Society of America, Decade of North American Geology, Volume A, pp. 97–138.